A Double-Pulsar System: A Rare Laboratory for Relativistic Gravity and Plasma Physics

A. G. Lyne,[1]* M. Burgay,[2] M. Kramer,[1] A. Possenti,[3,4] R.N. Manchester,[5] F. Camilo,[6] M. A. McLaughlin,[1] D. R. Lorimer,[1] N. D'Amico,[3,7] B. C. Joshi,[8] J. Reynolds,[9] P. C. C. Freire[10]

The clocklike properties of pulsars moving in the gravitational fields of their unseen neutron-star companions have allowed unique tests of general relativity and provided evidence for gravitational radiation. We report here the detection of the 2.8-second pulsar J0737−3039B as the companion to the 23-millisecond pulsar J0737−3039A in a highly relativistic double neutron star system, allowing unprecedented tests of fundamental gravitational physics. We observed a short eclipse of J0737−3039A by J0737−3039B and orbital modulation of the flux density and the pulse shape of J0737−3039B, probably because of the influence of J0737−3039A's energy flux on its magnetosphere. These effects will allow us to probe magneto-ionic properties of a pulsar magnetosphere.

Double neutron star (DNS) binaries are rare, and only six such systems are known. However, they can provide wonderful laboratories for the study of relativistic gravity and gravitational radiation (*1*). The discovery of such systems has been a prime objective of pulsar surveys since the first, PSR B1913+16, was discovered 29 years ago (*2*). Apart from their rarity, they are particularly difficult to find because of the large orbital acceleration experienced by the members of the systems, resulting in large and varying Doppler effects in the observed rotational period.

The pulsar J0737−3039 was recently identified as part of a high-latitude multibeam survey of the southern sky using the 64-m Parkes radio telescope (*3*). It was found to be in a 2.4-hour eccentric orbit with another compact object that the observed orbital parameters suggested was another neutron star. The short orbital period and compactness of the system and the high timing precision, made possible by the large flux density and narrow pulse features of this pulsar, promise to make this system a superb laboratory for the investigation of relativistic astrophysics. Relativistic advance of the angle of periastron has already been measured, and orbital decay due to gravitational wave emission will be measured with high precision within a few months. The resulting inspiral will end in coalescence of the two stars in about 85 million years (My) (*3*). This finding significantly increases the estimates of the detection rate of DNS inspirals by gravitational wave detectors (*3*, *4*).

The observation of PSR J0737−3039B. No other pulsar was detected in the 4.5-min discovery observation of PSR J0737−3039. However, analysis of data acquired subsequently for detailed studies of the system has revealed the occasional presence of pulsations with a period of 2.8 s. This pulsar, henceforth called PSR J0737−3039B (or simply B in this paper), has the same dispersion measure (the integrated column density of free electrons along the line of sight) as the original pulsar, henceforth called PSR J0737−3039A (or simply A), and shows Doppler variations in the pulse period that identify it as the companion.

The data obtained by Burgay *et al.* (*3*) for their studies of A used the Parkes radio telescope at a frequency of 1390 MHz and have now all been reprocessed to enable investigation of the properties of B. Additionally, the system was observed on 7 days in November 2003 simultaneously with dual-polarization receivers centered on frequencies of 680 MHz and 3030 MHz (*5*). Observations of both pulsars were also made at 1396 MHz with the 76-m Lovell telescope at Jodrell Bank, also with a dual-polarization receiver. Timing observations of both pulsars have been made covering the 7 months from May to November 2003, with individual data spans between 10 min and 5 hours.

The main features of the observations of B are shown in Fig. 1, which illustrates the strength of the 2.8-s pulsed emission in the three frequency bands as a function of orbital phase and pulse phase over the full orbit. Most notable is the variation in the received flux density of B, which is clearly visible for two brief periods of about 10 min in duration each and centered on orbital longitudes 210° and 280°. Within these bursts, the strength is such that most pulses are detected individually. In addition to the orbital phases where it is always detected, the pulsar often shows weak emission elsewhere, notably between orbital phases 0° and 20° (Fig. 1B). It is likely that observations with greater sensitivity will reveal more widespread emission throughout the orbit. The pattern of the visibility is essentially stable from orbit to orbit and from band to band over the full frequency range of 680 to 3030 MHz. The absence of pulsar B in the discovery observation of A can now be understood, because that observation was made at a longitude of 146°, where there is little emission from B.

There are significant changes in the shape of the pulses of B with orbital phase (Fig. 1). The data at 1390 MHz show that it varies from a narrow intense main pulse with a weak precursor in the burst around longitude 210° to a roughly equal double-component profile with a somewhat greater separation near longitude 280°. It becomes essentially a single pulse at around longitude 0°. There is also an indication of frequency evolution of pulse shape within the bursts. The double nature of the profiles becomes more evident at the higher frequency of 3030 MHz and less so at 680 MHz, where the components seem to have nearly merged.

In order to make timing measurements of B, a phase-dependent set of pulse templates was created by forming average profiles for each of the three burst regions. These templates were aligned in such a way that the trailing, usually more intense, components were at the same pulse phase. Cross-correlation of data with appropriate templates from this set was carried out to produce times of arrival (TOAs). These TOAs were then compared with a model for the astrometric, rotational, and orbital parameters with the use of the TEMPO pulsar timing program (*6*). The position and main orbital parameters have been determined from the high-precision timing enabled by the strong, narrow pulses of A (Table 1). For B, an offset of 180° was added to the longitude of perias-

[1]Jodrell Bank Observatory, University of Manchester, Macclesfield SK11 9DL, UK. [2]Dipartimento di Astronomia, Università degli Studi di Bologna, Via Ranzani 1, 40127 Bologna, Italy. [3]Osservatorio Astronomico di Cagliari, Istituto Nazionale di Astrofisica (INAF), Localita. Poggio dei Pini, Strada 54, 09012 Capoterra, Italy. [4]Osservatorio Astronomico di Bologna, INAF, Via Ranzani 1, 40127 Bologna, Italy. [5]Australia Telescope National Facility (ATNF), Commonwealth Scientific and Industrial Research Organization (CSIRO), Post Office Box 76, Epping, New South Wales 1710, Australia. [6]Columbia Astrophysics Laboratory, Columbia University, 550 West 120th Street, New York, NY 10027, USA. [7]Dipartimento di Fisica, Università degli Studi di Cagliari, SP Monserrato-Sestu km 0.7, 09042 Monserrato, Italy. [8]National Centre for Astrophysics, Post Office Bag 3, Ganeshkhind, Pune 411007, India. [9]Parkes Observatory, ATNF, Post Office Box 276, Parkes, New South Wales 2870, Australia. [10]National Astronomy and Ionosphere Center, Arecibo Observatory, HC03 Box 53995, PR 00612, USA.

*To whom correspondence should be addressed. E-mail: agl@jb.man.ac.uk

tron, and the only fitted parameters were the pulsar rotational period, P, its first derivative, $\dot{P}$, and the projected semimajor axis, $x_B = a_B (\sin i)/c$, where i is the orbital inclination and c is the speed of light (Table 1).

Gravitational physics. With their strong gravitational fields and rapid motions, DNS binaries exhibit large relativistic effects. General relativity and other theories of gravity can be tested when a number of relativistic corrections, the so-called post-Keplerian (hereafter PK) parameters, to the classical Keplerian descriptions can be measured. In this formalism, for point masses with negligible spin contributions, the PK parameters in each theory should only be functions of the a priori unknown neutron star masses and the classical Keplerian parameters. With the two masses as the only free parameters, the measurement of three or more PK parameters overconstrains the system and thereby provides a test ground for theories of gravity (*7*). In a theory that describes the binary system correctly, the PK parameters define lines in a mass-mass diagram that all intersect in a single point. Such tests have been possible to date in only two DNS systems, pulsar (PSR) B1913+16 (*8*) and PSR B1534+12 (*9*) [see also (*10*)]. For PSR B1913+16, the relativistic periastron advance, $\dot{\omega}$, the orbital decay due to gravitational wave damping, $\dot{P}_b$, and the gravitational redshift and time dilation parameter, γ, have been measured, providing a total of three PK parameters. For PSR B1534+12, Shapiro delay (*11*), caused by passage of the pulses through the gravitational potential of the companion, is also visible, because the orbit is seen nearly edge-on. This results in two further PK parameters, r ("range") and s ("shape") of the Shapiro delay. However, the observed value of $\dot{P}_b$ requires correction for kinematic effects (*12*), so that PSR B1534+12 provides four PK parameters usable for precise tests (*9*).

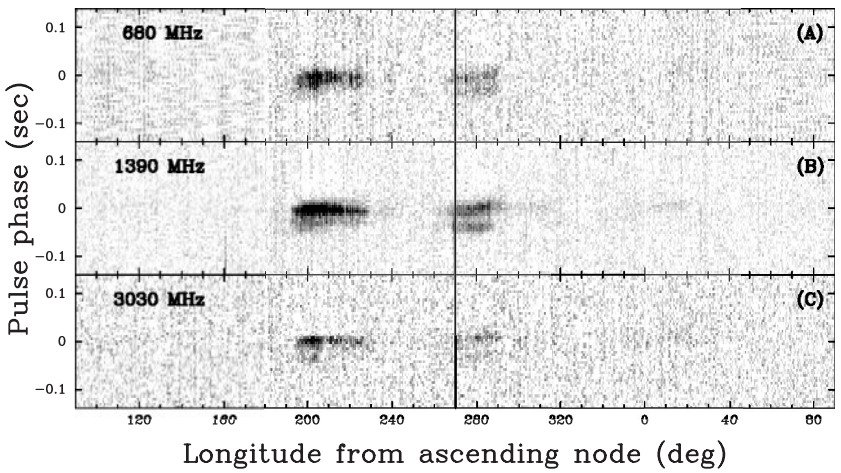

Fig. 1. The intensity of radiation of B as a function of orbital longitude relative to the ascending node of its orbit. Each panel shows a gray plot of intensity over a phase range of 0.1 of pulsar rotational period, centered on the pulsed emission. (**A**), (**B**), and (**C**) present observations at 680 MHz, 1390 MHz, and 3030 MHz, respectively (summed over six orbits at 1390 MHz and two orbits at each of the other frequencies), showing the similarity of the intensity variation over the wide frequency range and the changing pulse shape with orbital longitude. Longitude in this diagram (and in Figs. 2 and 5) is strictly the sum of the longitude of periastron and the true anomaly. The vertical line at longitude 270° represents the longitude of inferior conjunction of B, when the two stars are at their closest on the sky and B is the nearer to the Earth. deg., degree; sec, second.

Table 1. Observed and derived parameters of PSRs J0737−3039A and B with the use of the DD timing model (*11*, *13*). Standard (1 σ) errors are given in parentheses after the values and are in units of the least significant digit(s). The parameters *A*, *B*, and δ_r in the DD model were assumed to be zero in the analysis. The distance is estimated from the dispersion measure and a model for the interstellar free electron distribution (*32*). Dash entries indicate assumed values as measured for A; blank entries indicate not measured. h, hours; m, minutes; s, seconds.

	PSR J0737−3039A	PSR J0737−3039B
Pulse period P (ms)	22.69937855615 (6)	2773.4607474 (4)
Period derivative $\dot{P}$	1.74×10^{-18} (0.05×10^{-18})	0.88×10^{-15} (0.13×10^{-15})
Epoch of period (MJD)	52870.0	52870.0
Right ascension (J2000)	$07^h37^m51^s.247$ (2)	–
Declination (J2000)	−30°39′40″.74 (3)	–
Dispersion measure DM (cm^{-3} pc)	48.9 (2)	48.7 (2)
Orbital period P_b (day)	0.102251563 (1)	–
Eccentricity e	0.087779 (5)	–
Epoch of periastron T_0 (MJD)	52870.0120589 (6)	–
Longitude of periastron ω (deg)	73.805 (3)	73.805 + 180.0
Projected semimajor axis $x = a (\sin i)/c$ (s)	1.41504 (2)	1.513 (4)
Advance of periastron $\dot{\omega}$ (degree/year)	16.90 (1)	–
Gravitational redshift parameter γ (ms)	0.38 (5)	
Shapiro delay parameter s	0.9995 (−32, +4)	
Shapiro delay parameter r (μs)	5.6 (−12, +18)	
Root mean square timing residual (μs)	27	2660
Flux density at 1390 MHz (mJy)	1.6 (3)	0–1.3 (3)
Characteristic age τ (My)	210	50
Surface magnetic field strength B (Gauss)	6.3×10^9	1.2×10^{12}
Spin-down luminosity $\dot{E}$ (erg/s)	6000×10^{30}	2×10^{30}
Mass function ($M_\odot$)	0.29097 (1)	0.356 (3)
Distance (kpc)	~0.6	
Total system mass $m_A + m_B$ ($M_\odot$)	2.588 (3)	
Mass ratio $R \equiv m_A/m_B$	1.069 (6)	
Orbital inclination from Shapiro s (degree)	87 (3)	
Orbital inclination from (R, $\dot{\omega}$) (degree)	87.7 (−29, +17)	
Stellar mass from (R, $\dot{\omega}$) ($M_\odot$)	1.337 (5)	1.250 (5)

Extending and improving the timing solution for A (*3*), we have measured A's $\dot{\omega}$ and γ and have also detected the Shapiro delay in the pulse arrival times of A due to the gravitational field of B (Fig. 2). This provides four measured PK parameters, resulting in a $m_A - m_B$ plot (Fig. 3) through which we can test the predictions of general relativity (*11*, *13*). However, the detection of B as a pulsar opens up opportunities to go beyond what is possible with previously known DNS binary systems. First, we can exclude all regions in the $m_A - m_B$ plane that are forbidden by the individual mass functions of A and B because of the requirement $\sin i \leq 1$. Secondly, with a measurement of the projected semimajor axes of the orbits of A and B (Table 1), we obtain a precise measurement of the mass ratio, $R(m_A, m_B) \equiv m_A/m_B = x_B/x_A$, providing a further constraint in the $m_A - m_B$ plot (Fig. 3). This relation is valid for any theory of gravity (*7*, *14*). Most importantly, the R line is independent of strong-field (self-field) effects, providing a stringent and new constraint for tests of gravitational theories (*11*, *13*, *15*).

With four PK parameters already available for tests, this additional constraint makes this system the most overdetermined DNS binary to date and a truly unique laboratory for relativistic gravity. Moreover, with a significant measurement of $\dot{P}_b$ expected within the next few months, an additional PK parameter will become available. This may provide a sixth constraint if kinematic effects are

negligible or can be isolated by proper motion and distance measurements. The position of the allowed region in Fig. 3 also determines the inclination of the orbit to the line of sight. It turns out that the system is observed nearly edge-on, with an inclination angle i of about 87° (Table 1).

Because of the curvature of space-time near massive objects, the spin axes of both pulsars will precess about the total angular momentum vector, changing the orientation of the pulsars as seen from Earth (*16*). With the measured system parameters (Table 1), general relativity predicts periods of such geodetic precession of only 75 years for A and 71 years for B (*17*). Hence, the relative orientation of the pulsars' spin axes within the system geometry is expected to change on short time scales. This should lead to measurable changes in the profiles of A and B [compare with (*18*–*20*)] and perhaps also to measurable changes in the aberration effects because of the rotation of A and B. Hence, we can expect that additional PK parameters can be measured that are too small to be detected in other binary pulsars. Some examples of these are the aberration terms A, B, and δ_r in the Damour and Dervelle (*11*, *13*) timing model (DD model) that we used, assumed to be zero for the present analysis.

In contrast to previous tests of general relativity, we may soon have to use higher order terms than $(v/c)^2$ to describe the system accurately, the first time this has been necessary for binary pulsar systems. The future high precision of the measurement of $\dot{\omega}$ may demand this first for comparison of the observed value of this parameter with theories of gravity (*21*). Deviations from the value predicted by general relativity may be caused by contributions from spin-orbit coupling (*17*), which is about an order of magnitude larger than that for PSR B1913+16. This potentially will allow us to measure the moment of inertia of a neutron star for the first time (*21*, *22*).

Origin and evolution of the double-pulsar system. The existence of DNS binaries can be understood by a binary evolution scenario that starts with two main-sequence stars [e.g., (*23*)]. The initially more massive star evolves first and eventually explodes in a supernova to form a neutron star. Under favorable conditions, this neutron star remains bound to its companion and spins down as a normal pulsar for the next 10^6 to 10^7 years. At some later time, the remaining (secondary) star comes to the end of its main-sequence lifetime and begins a red giant phase. Depending on the orbital parameters of the system, the strong gravitational field of the neutron star attracts matter from the red giant, forming an accretion disk and making the system visible as an x-ray binary. The accretion of matter transfers orbital angular momentum to the neutron star, spinning it up to short periods and dramatically reducing its magnetic field (*24*, *25*). A limiting spin period is reached because of equilibrium between the magnetic pressure of the accreting neutron star and the ram pressure of the infalling matter (*23*, *26*).

A crucial phase in the evolution of close DNS binaries like J0737−3039 is the dramatic reduction in orbital separation that occurs when matter from the secondary star is expelled from the system, resulting in a very compact system consisting of a helium star and a neutron star (*27*, *28*). A sufficiently massive helium star will ultimately undergo a supernova explosion, forming a young second neutron star. If the stars remain bound after this explosion, the resulting system is a pair of neutron stars in an eccentric orbit with very different magnetic field strengths and hence spin-down properties, as in fact observed here. With masses of $m_A = 1.34\ M_\odot$ and $m_B = 1.25\ M_\odot$, A is typical of other neutron stars with measured masses (*10*, *29*), whereas B has a significantly smaller mass than any other.

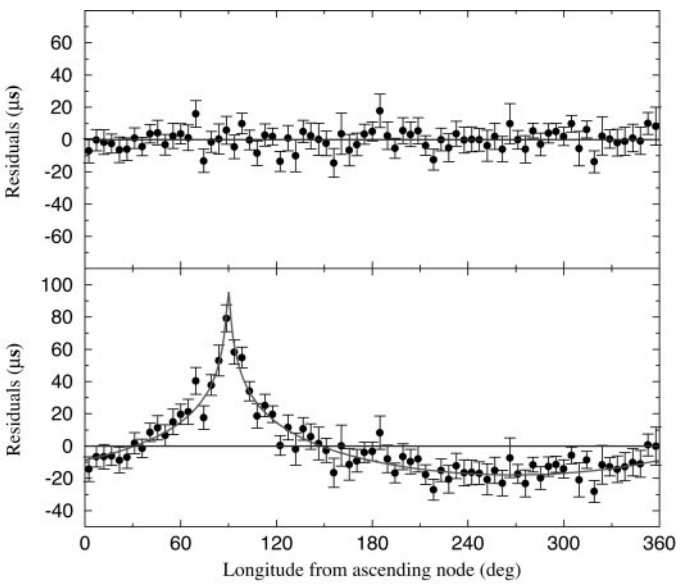

Fig. 2. The effect of the Shapiro delay caused by the gravitational potential of B seen in the timing residuals of A. Residuals were averaged into 75 equal bins of orbital longitude. (**Top**) Timing residuals obtained by subtracting the model defined in Table 1 from the observed TOAs. (**Bottom**) As top display, but with the Shapiro delay parameters r and s set to zero.

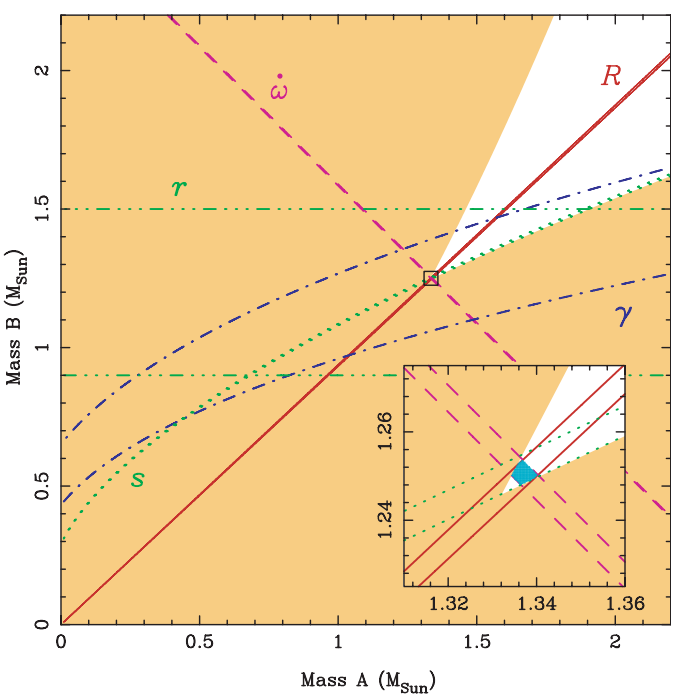

Fig. 3. The observational constraints on the masses m_A and m_B. The colored regions are those that are excluded by the Keplerian mass functions of the two pulsars. Further constraints are shown as pairs of lines enclosing permitted regions as predicted by general relativity: (i) the measurement of the advance of periastron $\dot{\omega}$, giving the total mass $m_A + m_B = 2.588 \pm 0.003\ M_\odot$ (dashed line); (ii) the measurement of $R \equiv m_A/m_B = x_B/x_A = 1.069 \pm 0.006$ (solid line); (iii) the measurement of the gravitational redshift and time dilation parameter γ (dot-dash line); (iv) the measurement of Shapiro parameter r giving $m_B = 1.2 \pm 0.3\ M_\odot$ (dot-dot-dot-dash line); and (v) Shapiro parameter s (dotted line). **Inset**) An enlarged view of the small square that encompasses the intersection of the three tightest constraints, with the scales increased by a factor of 16. The permitted regions are those between the pairs of parallel lines, and we see that an area exists which is compatible with all constraints, delineated by the solid blue region.

The time since the second supernova explosion can be estimated by comparing our measurements of P and $\dot{P}$ for A and B, which can be used to compute their characteristic ages $\tau = P/(2\dot{P})$. If characteristic ages are good indicators of pulsars' true ages, we expect $\tau_A = \tau_B$, but the observed values are $\tau_A \cong 4\tau_B$. This discrepancy can be reconciled by questioning one or more of the assumptions inherent in the use of characteristic ages as estimates of true ages: a negligible birth spin period and a nondecaying magnetic dipole braking torque. At the very least, the postaccretion spin period of A cannot have been negligible because of details of the accretion process discussed above. Simple models assuming constant magnetic dipole spin-down (*26*) predict a postaccretion spin period for A in the range of 10 to 18 ms, enough to explain the observed discrepancy in the characteristic ages.

Probing pulsar magnetospheres. The separation of the two pulsars in their orbits (Fig. 4, top) is typically ~900,000 km or 3 light-s (that is, the distance light travels in 3 s). The large orbital inclination means that, at conjunction, the line of sight to one pulsar passes within about 0.15 light-s of the other (Fig. 4, bottom). This is substantially smaller than the 0.45-light-s radius of B's light cylinder, the point at which the corotation speed equals the speed of light, although much greater than the 0.004–light-s light-cylinder radius of A. As the pulsars move in their orbits, the line of sight from A passes through and sweeps across the magnetosphere of B, providing the opportunity to probe its physical conditions. The determination of changes in the radio transmission properties, including the dispersion and rotation measures, will potentially allow the plasma density and magnetic field structure to be probed. Additionally, the ~70-year period geodetic precession will cause the line of sight to sample different trajectories through the magnetosphere of B. To a lesser extent, the 21-year orbital precession will also cause changes in the trajectory.

Close inspection of the flux density of the pulses from A (Fig. 5) reveals that a short occultation occurs, centered on its superior conjunction (when the line of sight passes only 0.15 light-s from B). The duration of the occultation is about 20 to 30 s. Because the relative transverse velocity is about 660 km s^{-1}, the eclipsing region has a lateral extent of ~15,000 km or ~0.05 light-s, about 10% of the light-cylinder radius of B. As far as we can tell at present, the eclipse occurs in every orbit, and its extent is essentially the same at 680 MHz and 1390 MHz, limiting the possible interpretations. One clue may come from the fact that the rate of spin-down energy loss from A is 3000 times greater than that from B. In fact, at the light-cylinder radius of B, the energy density of the relativistic wind from A is about two orders of magnitude greater than that from B, ensuring that the wind from A will penetrate deep into B's magnetosphere. We find that the energy densities due to the spin-down luminosity (assumed isotropic) emitted by A and the magnetic field of B are in balance at a distance ~0.2 light-s from B, about 40% of the light-cylinder radius of B, assuming that the magnetic field can be calculated with the use of the standard dipole formula (*30*). Within this distance, the energy field of B will dominate, whereas A will dominate outside. Even though this picture is roughly consistent with the lateral extent of the observed eclipse of A, it is likely that the strong departure of B's magnetosphere from an ideal case makes such calculations uncertain.

Because the point of pressure balance is deep within the magnetosphere of B, the actual penetration of the wind from A into B's magnetosphere will be a function of the orientation of the rotation and/or magnetic axes of B relative to the direction of the wind and hence will depend on the precessional and orbital phases of B. This is the most likely explanation for the large flux density and pulse-shape changes of B, which are seen to vary with orbital phase (Fig. 1). We note that these changes are essentially the same between 680 and 3030 MHz. It seems most likely to us that such a broadband modulation arises from the impact of energy, in the form of particles, gamma rays, or 44-Hz electromagnetic radiation, from the millisecond pulsar A upon the magnetosphere of B. We note that there is a strong indication of significant unpulsed radio emission from the system:

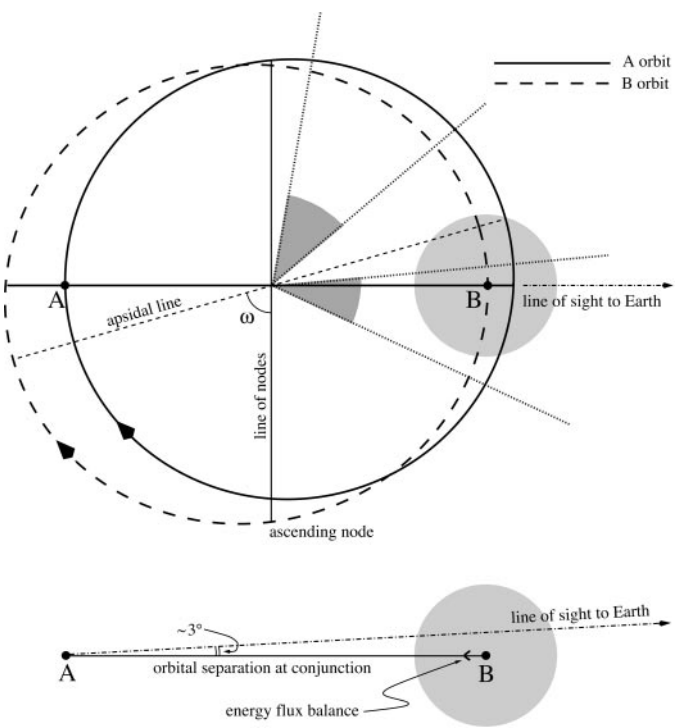

Fig. 4. The physical configuration of the binary system, at conjunction, as on 19 August 2003 [modified Julian date (MJD) 52870], showing the relative sizes of the two orbits and B's magnetosphere. At conjunction, the two neutron stars are separated by ~2.8 light-s or about 800,000 km. (**Top**) View from above the orbital plane with the Earth to the right. The shaded segments indicate orbital phases where B is detected strongly (see Fig. 1). The apsidal line is the major axis of the orbits, and the line of nodes is the intersection of the orbital plane and the plane through the center of mass of the system, which is normal to the line of sight. (**Bottom**) View from the side, showing the passage of the line of sight from A to the Earth through the magnetosphere of B. The approximate position of the pressure balance between the relativistic wind from A and the magnetic field of B is indicated.

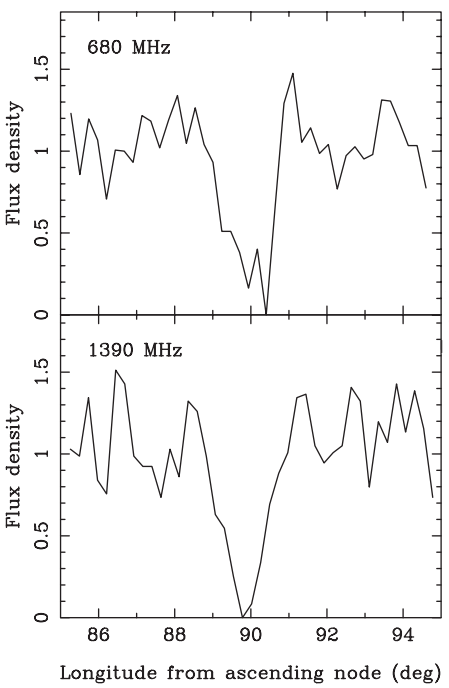

Fig. 5. The variation in flux density of A (in arbitrary units) at 680 and 1390 MHz, around superior conjunction (i.e., longitude 90°). The data are presented with 5-s time resolution and show the eclipse of the pulsar by the magnetosphere of B.

The time-averaged pulsed flux density of the pulsars is about 1.8 mJy (1 Jy = 10^{-26} W m^{-2} Hz^{-1}) at 1390 MHz (Table 1), compared with a total flux density at this frequency of 7 mJy (*3*). The ~5-mJy unpulsed emission probably arises in the impact region described above. We find it remarkable, with much of the magnetosphere of B blown away by the wind of A, that B still works as a pulsar. This suggests that the radio emission is probably generated close to the neutron star, providing a direct constraint on the emission height.

Conclusion. We have detected the binary companion of the millisecond pulsar J0737−3039 as a pulsar, making this the first known double-pulsar system. This discovery confirms the neutron-star nature of the companions to recycled pulsars in eccentric binary systems and validates the suggested evolutionary sequences in which a companion star, having spun up the pulsar, forms a young pulsar in a supernova explosion (*31*). The highly relativistic nature of this compact system opens up opportunities for much more stringent tests of relativistic gravitation than have been possible previously. Not only have we already measured four quantities attributable to, and consistent with, general relativity, but the mass ratio R is a new high-precision constraint that is independent of gravitational theories. Within a year or so, we expect to measure the orbital decay due to emission of gravitational radiation. If the intrinsic value due to gravitational-wave damping can be extracted, it will allow tests of radiative aspects of gravitational theories mixed with strong-field effects. On somewhat longer time scales of a few years, we expect to detect several other relativistic effects, such as geodetic precession of the pulsars' spin axes, spin-orbit coupling, and other deviations, making this a superb test bed for relativity.

The detection of the companion as a pulsar also opens up the possibility of using each pulsar to probe the magnetosphere of the other. The energy flux from the millisecond pulsar is strongly affecting the pulse emission process in the companion, and eclipses of the millisecond pulsar by the companion are also seen. Future measurements of orbital variations in pulse shapes, amplitudes, polarization, and timing over a range of radio frequencies will give fascinating insights into magnetospheric processes in pulsars.

References and Notes

1. J. H. Taylor, *Philos. Trans. R. Soc. London Ser. A* **341**, 117 (1992).
2. R. A. Hulse, J. H. Taylor, *Astrophys. J.* **195**, L51 (1975).
3. M. Burgay *et al.*, *Nature* **426**, 531 (2003).
4. V. Kalogera *et al.*, *Astrophys. J.*, in press; preprint is available at http://arxiv.org/abs/astro-ph/0312101.
5. Receiver bandwidths used were 64 MHz at 680 MHz, 256 MHz at 1390 MHz, and 576 MHz at 3030 MHz.
6. More information is available at http://pulsar.princeton.edu/tempo/.
7. T. Damour, J. H. Taylor, *Phys. Rev. D* **45**, 1840 (1992).
8. J. H. Taylor, J. M. Weisberg, *Astrophys. J.* **345**, 434 (1989).
9. I. H. Stairs, S. E. Thorsett, J. H. Taylor, A. Wolszczan, *Astrophys. J.* **581**, 501 (2002).
10. M. Bailes, S. M. Ord, H. S. Knight, A. W. Hotan, *Astrophys. J.* **595**, L49 (2003).
11. T. Damour, N. Deruelle, *Ann. Inst. Henri Poincaré* **44**, 263 (1986).
12. T. Damour, J. H. Taylor, *Astrophys. J.* **366**, 501 (1991).
13. T. Damour, N. Deruelle, *Ann. Inst. Henri Poincaré* **43**, 107 (1985).
14. This is correct up to so-called first post-Newtonian [$(v/c)^2$] order (*7*), and any intersection of the PK-parameter lines must be located on the R line, which will only deviate from that shown in Fig. 3 by corrections of order $(v/c)^4$.
15. This is correct because of the usage of the DD timing model in our analysis and its definition of mass (*11*, *13*).
16. T. Damour, R. Ruffini, *C. R. Acad. Sci. Paris Ser. A* **279**, 971 (1974).
17. B. M. Barker, R. F. O'Connell, *Astrophys. J.* **199**, L25 (1975).
18. J. M. Weisberg, R. W. Romani, J. H. Taylor, *Astrophys. J.* **347**, 1030 (1989).
19. J. M. Weisberg, J. H. Taylor, *Astrophys. J.* **576**, 942 (2002).
20. M. Kramer, *Astrophys. J.* **509**, 856 (1998).
21. T. Damour, G. Schäfer, *Nuovo Cimento* **101**, 127 (1988).
22. N. Wex, *Class. Quantum Gravity* **12**, 983 (1995).
23. D. Bhattacharya, E. P. J. van den Heuvel, *Phys. Rep.* **203**, 1 (1991).
24. G. S. Bisnovatyi-Kogan, B. V. Komberg, *Sov. Astron.* **18**, 217 (1974).
25. N. Shibazaki, T. Murakami, J. Shaham, K. Nomoto, *Nature* **342**, 656 (1989).
26. Z. Arzoumanian, J. M. Cordes, I. Wasserman, *Astrophys. J.* **520**, 696 (1999).
27. E. P. J. van den Heuvel, C. de Loore, *Astron. Astrophys.* **25**, 387 (1973).
28. B. P. Flannery, E. P. J. van den Heuvel, *Astron. Astrophys.* **39**, 61 (1975).
29. S. E. Thorsett, D. Chakrabarty, *Astrophys. J.* **512**, 288 (1999).
30. R. N. Manchester, J. H. Taylor, Pulsars (Freeman, San Francisco, 1977).
31. G. Srinivasan, E. P. J. van den Heuvel, *Astron. Astrophys.* **108**, 143 (1982).
32. J. H. Taylor, J. M. Cordes, *Astrophys. J.* **411**, 674 (1993).

33. We would like to thank J. Sarkissian and other members of the Parkes multibeam team for their kind help with making the observations described in this paper and N. Wex and G. Schäfer for useful discussions. Extensive use was made of the PSRCHIVE pulsar analysis system developed by A. Hotan and colleagues (see http://astronomy.swin.edu.au/pulsar). The Parkes radio telescope is part of the Australia Telescope, which is funded by the Commonwealth of Australia for operation as a National Facility managed by CSIRO. M.B., A.P., and N.D. acknowledge financial support from the Italian Ministry of University and Research (MIUR) under the national program Cofin 2001. F.C. is supported by NSF, NASA, and National Radio Astronomy Observatory. D.R.L. is a University Research Fellow funded by the Royal Society.

12 December 2003; accepted 30 December 2003
Published online 8 January 2004;
10.1126/science.1094645
Include this information when citing this paper.

Empathy for Pain Involves the Affective but not Sensory Components of Pain

Tania Singer,[1]* Ben Seymour,[1] John O'Doherty,[1] Holger Kaube,[2] Raymond J. Dolan,[1] Chris D. Frith[1]

Our ability to have an experience of another's pain is characteristic of empathy. Using functional imaging, we assessed brain activity while volunteers experienced a painful stimulus and compared it to that elicited when they observed a signal indicating that their loved one—present in the same room—was receiving a similar pain stimulus. Bilateral anterior insula (AI), rostral anterior cingulate cortex (ACC), brainstem, and cerebellum were activated when subjects received pain and also by a signal that a loved one experienced pain. AI and ACC activation correlated with individual empathy scores. Activity in the posterior insula/secondary somatosensory cortex, the sensorimotor cortex (SI/MI), and the caudal ACC was specific to receiving pain. Thus, a neural response in AI and rostral ACC, activated in common for "self" and "other" conditions, suggests that the neural substrate for empathic experience does not involve the entire "pain matrix." We conclude that only that part of the pain network associated with its affective qualities, but not its sensory qualities, mediates empathy.

Human survival depends on the ability to function effectively within a social context. Central to successful social interaction is the ability to understand others intentions and beliefs. This capacity to represent mental states is referred to as "theory of mind" (*1*) or the ability to "mentalize" (*2*). Empathy, by contrast, broadly refers to being able to understand what others feel, be it an emotion or a sensory state. Accordingly, empathic experience enables us to understand what it feels like when someone else experiences sadness or happiness, and also pain, touch, or tickling (*3*).

Even though empathy has been extensively discussed and investigated by philosophers and social scientists, only recently has it become a focus for neuroscience (*3*–*8*). Influenced by perception-action models of motor behavior and imitation (*9*),

[1]Wellcome Department of Imaging Neuroscience, Institute of Neurology, University College of London, 12 Queen Square, WC1N 3AR London, UK. [2]Headache Group, Institute of Neurology, University College of London, Queen Square, WC1N 3BG London, UK.

*To whom correspondence should be addressed. E-mail: t.singer@fil.ion.ucl.ac.uk